3D GPS velocity field and its implications on the present-day post-orogenic deformation of the Western Alps and Pyrenees

Hai Ninh Nguyen[1], Philippe Vernant[1], Stephane Mazzotti[1], Giorgi Khazaradze[2], Eva Asensio[2]

[1]Laboratoire Géosciences Montpellier, Université Montpellier, Montpellier, France
5 [2]Grup Risknat, Departament de Geodinàmica i Geofísica, Facultat de Geologia, Universitat de Barcelona (UB), Martí i Franquès s/n, 08028 Barcelona, Spain

Correspondence to: Philippe Vernant (philippe.vernant@umontpellier.fr)

Abstract. We present a new 3D GPS velocity solution for 182 sites for the region encompassing the Western Alps, Pyrenees, and southern France. The velocity field is based on a Precise Point Positioning (PPP) solution, to which we apply a 10 common-mode filter, defined by the 26 longest time series, in order to correct for network-wide biases (reference frame, environmental noise, …). We show that processing options, such as troposphere delay, can lead to systematic velocity variations of 0.1 – 0.5 mm/yr affecting both accuracy and precision, especially for short (< 5 yr) time series. A velocity convergence analysis shows that minimum time-series lengths of ~3 years and ~5.5 years are required to reach a velocity stability of 0.5 mm/yr in the horizontal and vertical components, respectively. On average, horizontal residual velocities 15 show a stability of ~0.2 mm/yr in the Western Alps, Pyrenees, and southern France. The only significant horizontal strain rate signal is in the western Pyrenees with up to 4×10^{-9} yr^{-1} NNE-SSW extension, whereas no significant strain rates are detected in the Western Alps (< 1×10^{-9} yr^{-1}). In contrast, we identify significant uplift rates up to 2 mm/yr in the Western Alps but not in the Pyrenees (0.1 ± 0.2 mm/yr). A correlation between site elevations and fast uplift rates in the northern part of the Western Alps, in the region of the Wurmian ice cap, suggests that part of this uplift is induced by postglacial rebound. 20 The very slow uplift rates in the southern Western Alps and in the Pyrenees could be accounted for by erosion-induced rebound.

Keywords: Western Alps, Pyrenees, GPS, uplift, horizontal strain rates.

1 Introduction

25 The southwest European and Mediterranean domains are part of the broad plate boundary zone that accommodates the relative motion between the Nubian and Eurasian plates. In this domain, active tectonics in the Western Alps and Pyrenees mountains are revealed by a moderate level of seismic activity, geological evidences for Quaternary deformation, and sparse geomorphological observations of recent deformation (e.g., Alasset and Meghraoui, 2005; Chardon et al., 2005; Chevrot et al., 2011; Lacan and Ortuño, 2012; Larroque et al., 2009). Global Positioning System (GPS) data show that central

Europe east of the Rhine Graben and north of the Alps behaves rigidly at ~0.4 mm/yr and defines a stable Europe reference frame (e..g., Altamimi et al., 2011; Nocquet and Calais, 2003). To first order, horizontal deformation across the Alps and the Pyrenees is unresolvable at the level of GPS uncertainty, ~0.5 mm/yr (Nocquet, 2012; Rigo et al., 2015; Vigny et al., 2002), although recent studies suggest small possible extension in the French Alps (Walpersdorf et al., 2015) and the

5   western Pyrenees (Asensio et al., 2012; Rigo et al., 2015). In contrast, studies of vertical velocities from GPS data indicate significant uplift rates in the Western and Central Alps (up to ~2 mm/yr), decreasing toward the Eastern Alps (Serpelloni et al., 2013).

These very slow deformation rates in a stable plate context highlight the importance of characterization and quantification of

10   GPS velocity uncertainties. Numerous sources of uncertainties affect GPS velocity estimations, especially in the vertical component: e.g., reference frame errors (Argus et al., 1999), seasonal signals (Blewitt and Lavallée, 2002), atmospheric loading effects (Tregoning and Watson, 2009). These various sources of noise and non-tectonic signals can result in artificial trends over several years and systematic biases that may be correlated over large regions. Western Europe, as a near-stable region associated with low-deformation tectonic zones, provides an interesting test case to study GPS velocity

15   and uncertainty estimations. Can tectonic velocities, likely below 1 mm/yr, be resolved for the Western Alps and the Pyrenees mountains? Can uplift patterns in these two mountain belts help constrain studies of ongoing tectonics and dynamics (e.g, Champagnac et al., 2007; Fox et al., 2015; Genti et al., 2015; Vernant et al., 2013)?

In this study, we analyze data from 182 permanent GPS stations located in France and Spain in order to characterize the

20   horizontal and vertical deformation patterns in the Western Alps and Pyrenees. We focus on estimations of velocity uncertainties, mainly related to processing options and parameters, to define the minimum time span required to reach a set of horizontal and vertical velocity precision thresholds. These results are used to derive regional velocity and strain rate patterns in our study region.

25   **2 GPS data and processing**

We perform an analysis of GPS data from 1997 to December 2013 and provide a self-consistent velocity solution for 182 stations between longitudes -5°E and 10°E and latitudes 41°N and 49°N, with time series from 1.9 to 16.0 yr (average 7.8 yr), cf. Figure 1. Our analysis comprises stations from the following networks and operators: International GNSS Service (IGS, 3 stations), European Permanent GNSS (EUREF, 20 stations), Topo-Iberia (3 stations), Red de Geodesia Activa de

30   Navarra (RGAN, 7 stations), Escuela Politécnica Superior de Huesca (EPSH, 1 station), La Xarxa CatNet de ICGC (6 stations), French Réseau National GPS (RENAG, 56 stations), and French Réseau GNSS Permanent (RGP,,86 stations); cf. Acknowledgement section for network and data references. Some of these networks include sites operated for geographic or

cadastral purposes and are not always geodetic-quality monuments. We omit two sites of the RENAG network (BURE and JANU) because of numerous interruptions that cause significant nonlinearity to the time series.

For data processing, we use the Precise Point Positioning (PPP) software developed by the Canadian Geodetic Survey of Natural Resources Canada (Héroux and Kouba, 2001). This CSRS-PPP version 1.5 software provides GPS float solutions

5   utilizing precise satellite orbits and clocks, satellite and receiver absolute antenna phase center (APC) mapping, tropospheric models (hydrostatic and wet delays, and mapping functions), solid Earth and ocean tide loading, and Earth rotation parameters. For our reference solution, we use IGS final products (Kouba, 2009) for satellite orbits and clocks, Earth rotation models, and phase mapping corrections for both satellite and ground-based antennas. We apply ocean-tide loading corrections based on the FES2004 model (Lyard et al., 2006). Tropospheric delays are estimated and corrected using

10 Vienna Mapping Functions (VMF1, Boehm et al., 2006) with 10° elevation cutoff angle, zenith delay estimated every 5 minutes, and gradients every 6 hours. A priori troposphere parameters are derived from the European Centre for Medium-Range Weather Forecasts (http://www.ecmwf.int/).

We tested several processing options in order to estimate their impact on daily coordinates and estimated velocities.
15 Comparisons with our reference solution show that the choice of tropospheric model has limited impact on final velocities. Using Global Mapping Functions (GMF) instead of VMF1 results in mean differences of 0.2 and less than 0.1 mm/yr in vertical and horizontal velocities, respectively. In contrast, the omission of Earth rotation models can result in significant impact in the PPP processing (Kouba, 2009). Our test solution without Earth rotation corrections yields horizontal and vertical velocities that vary from the reference solution by 0.3 and 0.5 mm/yr on average. Similarly, the choice of APC

20 mapping models can result in significant velocity variations. We illustrate this point by comparing a solution with the previous IGS model (igs05.atx, associated with IGS05 reference system, Rothacher and Schmid, 2006) with our reference solution that uses the current model (igs08.atx, associated with IGS08 reference system, Rebischung et al., 2012). North, east, and vertical velocities of these two solutions differ by 0.1, 0.3, and 0.5 mm/yr on average. These tests indicate that the choice of processing parameters can lead to systematic velocity variations of the order of 0.5 mm/yr, affecting primarily

25 short (< 5 yr) time series. Because the impacts of those parameter choices are dependent on the duration of the time series, the associated uncertainties affect both the velocity accuracies (e.g., whole network translations) and precisions (e.g., apparent relative motions between sites) and must be considered for tectonic analysis of GPS data, specially in extremely low deforming areas such as western Europe.

3 Time series analysis

30 ### 3.1 Time series model

Daily position time series are decomposed into a linear term (constant velocity), sine functions with annual and semi-annual periods, and offsets defined by antenna, dome, and receiver changes as well as a visual inspection of the series. For each

station north, east and vertical components, position time series are inverted using a least-square norm to find the best-fit amplitudes of all model parameters.

Uncertainties in GPS velocities are a function of the uncertainty in the positions, the length of the time series, the number of
5 data points, the presence of steps in the time series, and the noise model (Agnew, 1992; Williams, 2003). For each station component, we perform a spectral analysis to estimate the spectral index and amplitude of the colored noise in the time series. We then use the formulation of Williams et al. (2003) to calculate the standard error on the north, east, and vertical velocities. Spectral indices α for our analysis range between -0.4 and -1.1, with a mean value $\alpha = -0.7$, indicating that noise in our PPP time series consists primarily of a combination of white ($\alpha = 0$) and flicker ($\alpha = -1$) sources, with a very small
10 random-walk ($\alpha = -2$) contribution. Mean velocity standard errors are 0.5, 0.4, and 0.7 mm/yr in the north, east, and vertical components, with a direct dependence on time series length (cf. Section 4.1). This noise analysis is consistent with current estimations of noise type in GPS time series analyzed with PPP and double-difference software (e.g., Santamaría-Gómez et al., 2011).

15 **3.2 Reference frame**

Daily positions and velocities calculated from our PPP analysis are in a reference frame defined by the satellite orbits and clocks. For the time period of interest these frames follow the official products of the "IGS Reprocessing 1" (e.g., Collilieux et al., 2009) and vary between IGS05 (up to 2011/04/17), IGS08 (between 2011/04/17 and 2012/10/07), and IGb08 (after 2012/10/07). The transformations between these three reference frames are not null, which results in potential offsets in our
20 calculated positions. However, each processing group involved in the computation of the IGS products may not adopt synchronous model changes, resulting in variation in our time series that cannot be corrected by a single break (T. Herring, pers. comm., March 23rd 2015).

In order to correct for these possible biases, we adopt an empirical approach that consists in removing residual signals common to the whole network. We first calculate a common-mode filter by stacking the residuals of the time series (post
25 time-series model, cf. section 3.1) for a subset of the 26 stations with 10 years or more of data, 80% of data completeness, and a network-wide coverage. This filter is then subtracted from the original time series of all 182 stations to produce filtered series that are re-analyzed. Figure 2 shows the common-mode filter. We perform a statistical analysis to estimate the effectiveness of this method by estimating the amplitude of offsets in the time series forced at the IGS05 - IGS08 and IGS08 - Igb08 transition dates. For the original (non-filtered) data, significant offsets are estimated in all three components (about
30 1.5 – 3 mm on average, Table 1). In contrast, the filtered data result in much smaller offsets (0.1 – 0.9 mm, Table 1) that are not significant compared to their standard deviation. Thus, we consider that our filtered solution is essentially free from

reference frame variation problems. This analysis also highlights the importance of the new "Reprocessing 2" analysis currently on going within the IGS.

Velocities calculated after the common-mode filter procedure are aligned with a "network average" reference frame, which is not directly aligned with a specific International Terrestrial Reference Frame (ITRF) realization. Our analysis includes 8 stations of the core IGS network for which official positions and velocities are provided in the latest ITRF2008 (Altamimi et al., 2011). Time series for these stations range between 11 and 16 year-length, resulting in well-constrained velocities. A comparison of our velocities with those from ITRF2008 is given in Table 2. The mean differences in the north, east, and vertical components are within their standard errors (0.03 ± 0.10, 0.07 ± 0.17, 0.17 ± 0.30 mm/yr), indicating no significant difference between our solution and ITRF2008 at better than ~0.1 and ~0.2 mm/yr in the horizontal and vertical components, respectively.

4 Precisions and uncertainties on velocities

In order to assess the impact of time-series length on the estimated velocity for our PPP solution, we perform a convergence analysis for each site in which we compare the velocity computed using the full time-series length to velocities computed for a range of time-series lengths of 1 yr and more. We estimate the minimum time required for the time-varying velocities to be similar to the long-term velocities within four thresholds values (1.0, 0.5, 0.2 and 0.1 mm/yr). This analysis is performed by extending the analyzed data by time steps of 2 months, starting from both the beginning (forward) and end (backward) of the series. Figure 3 presents an example for station MTPL of velocity evolution as a function of the time-series length relative to the reference (full length) velocity. For this station, the short-term velocities can deviate from the full-length reference by 1 mm/yr or more for series shorter than 3 – 4 years.

The results of this analysis for the 44 stations with data longer than 10 yr are summarized in Figure 4. Convergence times for the filtered data are systematically shorter (by about 1 – 2 yr) compared to the original data, due to the removal of long-period non-tectonic signals. For example, the minimum time-series lengths required to reach a stability threshold of 0.5 mm/yr in the horizontal components are ~5 years and ~3 years for the original and filtered data, respectively. Similarly, the convergence time decreases from ~6.5 years to ~5.5 years in the vertical component. Convergence times estimated for a 0.1 mm/yr velocity threshold are probably a minimum as about half of the time series used for this estimation have a length approaching the convergence time.

Kierulf et al. (2013) performed a similar convergence analysis for ~140 GPS stations in Norway. They estimate convergence times of 3.0, 2.5, and 3.5 years for a velocity convergence threshold of 0.5 mm/yr in the north, east, and vertical components, respectively. These estimations are similar to ours for the horizontal components and shorter by about 2 years for the vertical. This shorter convergence times may be due to (1) a rougher time step (6 months vs. 1 month) that limits their time resolution and (2) inclusion of short (< 10 years) time series in their statistics, which biases the convergence time

estimations to shorter values. The effect of double-difference processing, intrinsically less noisy than our PPP solution, may also contribute to shorter convergence times.

Because it removes a significant long-period noise component from the time series, the common-mode filter also has a strong impact on the estimation of velocity standard errors. The velocity uncertainty analysis (section 3.1) performed on

5   filtered data yields spectral indices significantly smaller (mean value α = -0.45 vs. α = -0.7 for the original data) and thus whiter spectra. This effect is illustrated in Figure 5 on the spectra for station MTPL original and filtered data. A direct consequence of these whiter spectra is the reduction by a factor of ~2 of the mean north, east, and vertical velocity standard errors compared to the original data (i.e. 0.2, 0.2, and 0.3 mm/yr vs. 0.5, 0.4, and 0.7 mm/yr for the unfiltered data).

5 Velocity solution

10 On the basis of the analyses described above, we present a final GPS velocity field using the filtered data (Table 3). The velocities for 139 stations with time series longer than 5 years, which correspond to an average velocity precision (convergence threshold) of ~0.5 mm/yr or better and 1σ horizontal velocity uncertainties smaller than 0.5 mm/yr, are represented in Figure 6. We define a regional reference frame by minimizing the velocities of 61 sites over the whole network and with time series longer than 6 years (see Table 3). The mean values of the residual velocities are 0.1 and 0.06

15 mm/yr for the north and east component, respectively. This result is in agreement with previous studies (e.g. Altamimi et al., 2011; Argus et al., 2010; Nocquet and Calais, 2003; Nocquet, 2012) and shows that horizontal deformation is very slow, including in the Western Alps and Pyrenees. The only site with a large velocity (> 2 mm/yr) corresponds to a station of the foot of a landslide (CLAP, southwestern Alps).

Figure 7 shows the dispersion of the East and North components of the residual velocities. The 65 sites with time series

20 longer than 8 years, horizontal velocities are lower than 0.7 mm/yr (except CLAP) and the weighted root-mean-square (WRMS) dispersion is 0.18 mm/yr. For stations with longer time series of more than 10 or 12 years, the WRMS are similar (0.17 and 0.18 mm/yr, respectively). This stability of the dispersion for stations over 8 years raises the question of whether these velocities represent a long-term motion of the sites or if we are reaching the threshold of the GPS horizontal velocity accuracy.

25 Deformation patterns associated with our velocity field are estimated by running an interpolation and smoothing function through the 3D velocity data. Horizontal strain rates are calculated on a regular 0.5 x 0.5 degree grid using a Gaussian interpolation function with a 75 km half-width and taking into account each GPS sites uncertainty (cf., Mazzotti et al., 2011). The horizontal strain rate field (Figure 8) shows no significant strain rates above ~1 x 10^{-9} yr^{-1}, except in the western Pyrenees where north-south to northeast-southwest extension is observed up to ~4 x 10^{-9} yr^{-1}, above the formal uncertainty

30 level. This strain rate pattern is consistent with that derived from shorter time series of the Spanish continuous sites (Asensio et al., 2012) and campaign GPS data in the Pyrenees, where Rigo et al. (2015) estimate a north-south extension of ~2 x 10^{-9} yr^{-1} in the western region but no significant strain in the central and eastern regions. In contrast, our estimation of non-

significant strain rates (< 1 x 10^{-9} yr^{-1}) in the Western Alps does not agree with campaign GPS results in the Briançon region where east-west extension rates of (16 ± 11) x 10^{-9} yr^{-1} are estimated (Walpersdorf et al., 2015). This disagreement may be due to the high spatial wavelength of our solution (~100 km or more) whereas campaign data from Walpersdorf et al. (2015) sample a much smaller area (~30 km).

5   The main feature of the vertical velocities (Figure 9) is the zone of uplift (up to ~2.0 mm/yr) observed in the north-central region of the Western Alps. This pattern of uplift is clearly limited to the region north of about N 44.5°, whereas the southern French Alps and the foreland regions of the Rhone Valley and the French Jura show no vertical motion within ± 0.5 mm/yr. Our results are consistent with the uplift pattern identified by Serpelloni et al. (2013) in the Western Alps (average difference at common sites of 0.05 ± 0.79 mm/yr), although the higher station density in our solution allows a sharper

10   definition of region affected by significant uplift. In contrast, no significant vertical pattern can be observed in the Pyrenees, where most stations show vertical velocities about ± 0.5 mm/yr.

Stations in the northern region of the Western Alps show a first-order correlation between uplift rates and topography (Figure 10), with highest uplift rates (> 1.0 mm/yr) limited to stations located above ~1000 m altitude. This is consistent with GPS and leveling results in the Swiss Alps where the most elevated region displays uplift rates up to 2 mm/yr (Brockmann

15   et al., 2012). Although this correlation seems straightforward, it is not the altitude of the GPS site that matters, but the mean elevation of the mountains surrounding the site. In other words a GPS site in a valley located in the highest part of the western Alps should have a high uplift rate even if it is located at low elevation. Because GPS stations are commonly located on ridges rather than in valleys, station elevations are a good proxy for the mean elevation of the surrounding area. In the Western Alps, the southern part shows no evidences of significant uplift (~0 mm/yr), to the contrary of the northern part of

20   the Western Alps, where the uplift rates are the highest (1-2 mm/yr) for the same elevation range. To first order these uplift rates seems correlated to the Wurmiam ice cap that was thicker in the northern part of the Western Alps (Stocchi et al., 2005) and can be modeled according so (Chéry et al., 20016).

Stations in the Pyrenees show no such correlation, in particular for the sites with the longest time series and above an elevation of 1500 m, which show vertical velocities of ~0.1 ± 0.2 mm/yr (Figures 9 and 10). This very low uplift rate is in

25   agreement with an erosion-induced deformation in the Pyrenees (Genti et al., 2015). Figure 10 shows no correlation between vertical velocities and time series lengths for the Western Alps or the Pyrenees, but it clearly shows the Pyrenees's lack of continuous GPS sites at mid to high elevations.

To the question "are the Alps collapsing?" (Selverstone, 2005), we can answer "not in the sense of a post-orogenic collapse of the mountain range". Indeed, our GPS velocities show no significant (< 0.2 mm/yr) horizontal outward flowing

30   of the Western Alps. On the other hand, significant uplift of the northern part of the Western Alps is clearly observed. These vertical velocities seem correlated to the Wurmian ice cap thickness and suggest that part of the present-day uplift is related to postglacial rebound. Models of glacial isotactic rebound for the Alps suggest either a low amplitude and a large wavelength (Stocchi et al., 2005) or a very localized uplift due to the Little Ice Age glacier shrinkage (Barletta et al., 2006); both models are not consistent with the GPS observations that suggest a short wavelength and a large amplitude of

the uplift. The drawback of these models is that they consider a 1D-layered lithosphere, which is probably far from the truth given the geological history of the region. An evidence for a more complicated lithosphere is given by the seismicity below Switzerland where the earthquake maximum depth vary from ~30 km in the foreland to ~15 km below the range (Deichmann, 2003). This suggests a wedge of softer material in the lower crust below the Alps (Chéry et al., 2016), in

5   some way similar to the Andes of Patagonia where a localized uplift due to glacier mass changes is modeled based on a wedge of softer material in the continental lithosphere (Klemann et al., 2007). This does not exclude contributions from deep processes for part of the uplift (Fox et al., 2015) or erosion-induced rebound (Champagnac et al., 2007; Genti et al., 2015; Vernant et al., 2013). A careful and detailed model of the response to the Last Glacial Maximum of the Pyrenees and the Alps will certainly bring valuable new insights on post-orogenic mountain processes.

10   **6. Conclusion**

Our new GPS velocity solution based on 182 sites for the region encompassing the Western Alps, the Pyrenees, and southern France leads to 4 main conclusions:

1) These areas can be associated with as a stable region, within a dispersion (WRMS) of ~0.2 mm/yr on the horizontal velocities. However, even with this low dispersion, horizontal velocities, without a regional coherence, can still reach up to

15   0.7 mm/yr, raising the question of the significance of these velocities: are there local processes explaining these residuals or do they represent a bias in our uncertainty estimates?

2) Significant horizontal strain rates up to 4×10^{-9} yr^{-1} of NNE-SSW extension are evidenced in the Western Pyrenees, but none are seen in the Western Alps (i.e. $< 1 \times 10^{-9}$ yr^{-1}).

3) In contrast, significant uplift rates up to 2mm/yr are observed in the Western Alps but not in the Pyrenees where they are

20   close to 0.1 ± 0.2 mm/yr.

4) These significant uplift rates are observed in the northern part of the Western Alps. They are correlated to the mean elevation of the region surrounding the GPS sites, but this correlation is not true for the Pyrenees or the southern part of the Western Alps.

25   The observations of uplift rates, and lack of significant horizontal motion in the northern Western Alps, are correlated with the Wurmian ice cap thickness and tend to suggest that a large part of this uplift is induced by postglacial rebound from the Last Glacial Maximum associated with a wedge of softer material in the continental lithosphere below the Western Alps. Unfortunately, the GPS network is too sparse to characterize uplift in the Pyrenees, where we see significant horizontal strain rates. With a few more sites in this region we will be able, with a careful comparison between the Pyrenees, the southern and

30   northern regions of the Western Alps, to decipher the role of erosion, glacier mass changes and deep processes in the present day uplift rates of this mountain ranges.

Acknowledgements

We thank Natural Resources Canada for providing the CCRS-PPP software. Time series analysis was done with the R statistical software (http://www.r-project.org). GPS data used in this study were extracted from the following archives: RENAG (http://www.renag.resif.fr), IGS (http://www.igs.org), EUREF (http://www.epncb.oma.be), RGP (http://rgp.ign.fr),

5   Topo-Iberia (http://www.igme.es/TopoIberia/default.html), RGAN (http://www.navarra.es/appsext/rgan/default.aspx), EPSH (http://epsh.unizar.es/~serreta/huescagps.html), CATNET (http://catnet-ip.icc.cat). This work was supported by the Centre National de la Recherche Scientifique (CNRS – INSU), Languedoc-Roussillon Regional Authority (grant Chercheurs d'Avenir to P. Vernant), and the REseau SIsmologique & géodésique Français (RESIF). We thank all the people involved in the GPS site maintenance and data distribution for the stations used in this study.

References

Agnew, D. C.: The time-domain behaviour of power-law noises, Geophys. Res. Lett., 19(4), 333–336, 1992.

15   Alasset, P.-J. and Meghraoui, M.: Active faulting in the western Pyrénées (France): Paleoseismic evidence for late Holocene ruptures, Tectonophysics, 409(1-4), 39–54, doi:10.1016/j.tecto.2005.08.019, 2005.

Altamimi, Z., Collilieux, X. and Métivier, L.: ITRF2008: an improved solution of the international terrestrial reference frame, J Geod, 85(8), 457–473, doi:10.1007/s00190-011-0444-4, 2011.

Argus, D. F., Gordon, R. G., Heflin, M. B., Ma, C., Eanes, R. J., Willis, P., Peltier, W. R. and Owen, S. E.: The angular

20   velocities of the plates and the velocity of Earth's centre from space geodesy, Geophys. J. Int., 180(3), 913–960, doi:10.1111/j.1365-246X.2009.04463.x, 2010.

Argus, D. F., Peltier, W. R. and Watkins, M. M.: Glacial isostatic adjustment observed using very long baseline interferometry and satellite laser ranging geodesy, J. Geophys. Res., 104(B12), 29077–29093, 1999.

Asensio, E., Khazaradze, G., Echeverria, A., King, R. W. and Vilajosana, I.: GPS studies of active deformation in the

25   Pyrenees, Geophys. J. Int., 190(2), 913–921, doi:10.1111/j.1365-246X.2012.05525.x, 2012.

Barletta, V. R., Ferrari, C., Diolaiuti, G., Carnielli, T., Sabadini, R. and Smiraglia, C.: Glacier shrinkage and modeled uplift of the Alps, Geophys. Res. Lett., 33, L14307, doi:10.1029/2006GL026490, 2006.

Blewitt, G. and Lavallée, D.: Effect of annual signals on geodetic velocity, J. Geophys. Res., 107(B7), ETG_9–1–ETG_9–11, 2002.

30   Boehm, J., Werl, B. and Schuh, H.: Troposphere mapping functions for GPS and very long baseline interferometry from European Centre for Medium-Range Weather Forecasts operational analysis data, J. Geophys. Res.-Solid Earth, 111(B2), B02406, doi:10.1029/2005JB003629, 2006.

Brockmann, E., Ineichen, D., Marti, U., Schaer, S. and Schlatter, A.: Determination of Tectonic Movements in the Swiss Alps using GNSS and Levelling., vol. 136, pp. 689–695. 2012.

Champagnac, J. D., Molnar, P., Anderson, R. S., Sue, C. and Delacou, B.: Quaternary erosion-induced isostatic rebound in the western Alps, Geology, 35(3), 195–198, doi:10.1130/g23053a.1, 2007.

5   Chardon, D., Hermitte, D., Nguyen, F. and Bellier, O.: First paleoseismological constraints on the strongest earthquake in France (Provence) in the twentieth century, Geology, 33(11), 901, doi:10.1130/G21713.1, 2005.

Chéry, J., Genti, M., & Vernant, P. (2016). Ice cap melting and low-viscosity crustal root explain the narrow geodetic uplift of the Western Alps. *Geophys. Res. Lett.*, 1–8. http://doi.org/10.1002/2016GL067821

Chevrot, S., Sylvander, M. and Delouis, B.: A preliminary catalog of moment tensors for the Pyrenees, Tectonophysics,
10   510(1-2), 239–251, doi:10.1016/j.tecto.2011.07.011, 2011.

Collilieux, X., Altamimi, Z., Métivier, L., and van Dam, T., 2009, Quality assessment of GPS reprocessed Terrestrial Reference Frame, Amer. Geophys. Union Fall Meeting, San Francisco.

Deichmann, N.: Focal depths of earthquakes below Switzerland, Swiss Seismol Service ETH Zürich, 2003.

Fox, M., Herman, F., Kissling, E. and Willett, S. D.: Rapid exhumation in the Western Alps driven by slab detachment and
15   glacial erosion, Geology, 43(5), 379–382, doi:10.1130/G36411.1, 2015.

Genti, M., Chery, J., Vernant, P. and Rigo, A.: Impact of gravity forces and topography denudation on normal faulting in Central–Western Pyrenees: Insights from 2D numerical models, Comptes Rendus Geoscience, 1–11, doi:10.1016/j.crte.2015.08.004, 2015.

Héroux, P. and Kouba, J.: GPS Precise Point Positioning using IGS orbit pro- ducts, Physical Chemical Earth, 26(6-8), 573–
20   578, 2001.

Kierulf, H. P., Ouassou, M., Simpson, M. J. R. and Vestøl, O.: A continuous velocity field for Norway, J Geod, 87(4), 337–349, doi:10.1007/s00190-012-0603-2, 2013.

Klemann, V., Ivins, E. R., Martinec, Z. and Wolf, D.: Models of active glacial isostasy roofing warm subduction: Case of the South Patagonian Ice Field, J. Geophys. Res.-Solid Earth, 112(B9), B09405, doi:10.1029/2006JB004818, 2007.

25   Kouba, J.: A guide to using International GNSS Service (IGS) products, International GNSS Service. [online] Available from: https://igscb.jpl.nasa.gov/components/usage.html, 2009.

Lacan, P. and Ortuño, M.: Active Tectonics of the Pyrenees: A review, Journal of Iberian Geology, 38(1), doi:10.5209/rev_JIGE.2012.v38.n1.39203, 2012.

Larroque, C., Delouis, B., Godel, B. and Nocquet, J.-M.: Active deformation at the southwestern Alps–Ligurian basin
30   junction (France–Italy boundary): Evidence for recent change from compression to extension in the Argentera massif, Tectonophysics, 467(1-4), 22–34, doi:10.1016/j.tecto.2008.12.013, 2009.

Lyard, F., Lefevre, F., Letellier, T. and Francis, O.: Modelling the global ocean tides: modern insights from FES2004, Ocean Dynamics, 56(5-6), 394–415, doi:10.1007/s10236-006-0086-x, 2006.

Mazzotti, S., Leonard, L.J., Cassidy, J.F., Rogers, G.C., and Halchuk, S.: Seismic hazard in western Canada from GPS strain rates versus earthquake catalog: Journal of Geophysical Research: Solid Earth, v. 116, no. B12, p. B12310, doi: 10.1029/2011JB008213, 2011.

Nocquet, J. M. and Calais, E.: Crustal velocity field of the western Europe from permanent GPS array solutions, 1996-2001, Geophys. J. Int., 154, 72–88, 2003.

Nocquet, J.-M.: Tectonophysics, Tectonophysics, 579(C), 220–242, doi:10.1016/j.tecto.2012.03.037, 2012.

Rebischung, P., Schmid, R., Ray, J., 2011. Upcoming switch to IGS08/igs08. atx. IGSMAIL- 6354.

Rigo, A., Vernant, P., Feigl, K. L., Goula, X., Khazaradze, G., Talaya, J., Morel, L., Nicolas, J., Baize, S., Chéry, J. and Sylvander, M.: Present-day deformation of the Pyrenees revealed by GPS surveying and earthquake focal mechanisms until 2011, Geophys. J. Int., 201(2), 947–964, doi:10.1093/gji/ggv052, 2015.

Rothacher, M., Schmid, R., 2006. ANTEX: The antenna exchange format version 1.3. Format specifications, IGS Central Bureau, Pasadena.

Santamaría-Gómez, A., Bouin, M.-N., Collilieux, X. and Wöppelmann, G.: Correlated errors in GPS position time series: Implications for velocity estimates, J. Geophys. Res.-Solid Earth, 116(B1), B01405, doi:10.1029/2010JB007701, 2011.

Selverstone, J.: Are the Alps collapsing? Annu. Rev. Earth Planet. Sci., 33(1), 113–132, doi:10.1146/annurev.earth.33.092203.122535, 2005.

Serpelloni, E., Faccenna, C., Spada, G., Dong, D. and Williams, S. D.: Vertical GPS ground motion rates in the Euro-Mediterranean region: New evidence of velocity gradients at different spatial scales along the Nubia-Eurasia plate boundary, J. Geophys. Res. Solid Earth, 118(11), 6003–6024, doi:10.1002/2013JB010102, 2013.

Stocchi, P., Spada, G. and Cianetti, S.: Isostatic rebound following the Alpine deglaciation: Impact on the sea level variations and vertical movements in the Mediterranean region, Geophys. J. Int., 162(1), 137–147, doi:10.1111/j.1365-246X.2005.02653.x, 2005.

Tregoning, P. and Watson, C.: Atmospheric effects and spurious signals in GPS analyses, J. Geophys. Res.-Solid Earth, 114(B9), B09403, doi:10.1029/2009JB006344, 2009.

Vernant, P., Hivert, F., Chéry, J., Steer, P., Cattin, R. and Rigo, A.: Erosion-induced isostatic rebound triggers extension in low convergent mountain ranges, Geology, 41(4), 467–470, doi:10.1130/G33942.1, 2013.

Vigny, C., Chéry, J., Duquesnoy, T., Jouanne, F., Ammann, J., Anzidei, M., Avouac, J. P., Barlier, F., Bayer, R., Briole, P., Calais, E., Cotton, F., Duquenne, F., Feigl, K. L., Ferhat, G., Flouzat, M., Gamond, J. F., Geiger, A., Harmel, A., Kasser, M., Laplanche, M., Le Pape, M., Martinod, J., M x000E9 nard, G., Meyer, B., Ruegg, J. C., Scheubel, J. M., Scotti, O. and Vidal, G.: GPS network monitors the Western Alps' deformation over a five-year period: 1993-1998, J Geod, 76(2), 63–76, doi:10.1007/s00190-001-0231-8, 2002.

Walpersdorf, A., Sue, C., Baize, S., Cotte, N., Bascou, P., Beauval, C., Collard, P., Daniel, G., Dyer, H., Grasso, J. R., Hautecoeur, O., Helmstetter, A., Hok, S., Langlais, M., Ménard, G., Mousavi, Z., Ponton, F., Rizza, M., Rolland, L., Souami,

D., Thirard, L., Vaudey, P., Voisin, C. and Martinod, J.: Journal of Geodynamics, Journal of Geodynamics, 85, 58–65, doi:10.1016/j.jog.2015.02.001, 2015.

Williams, S. D. P.: The effect of coloured noise on the uncertainties of rates estimated from geodetic time series, Journal of Geodesy, 76(9-10), 483–494, doi:10.1007/s00190-002-0283-4, 2003.
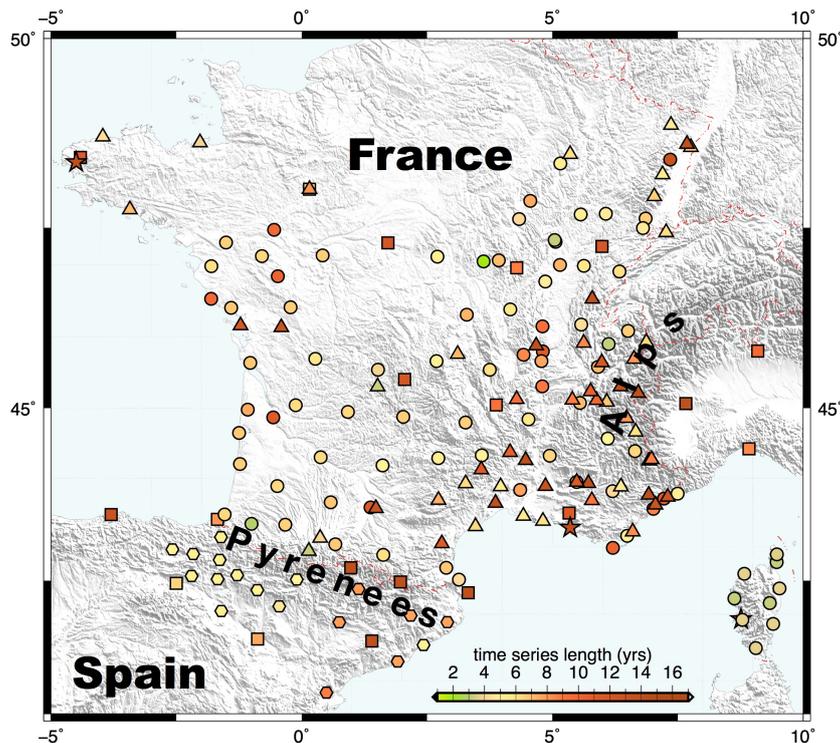
Figure 1: Distribution of the permanent stations used in this study. Symbols denote network (cf. text): Stars - IGS; Squares - EUREF-EPN; Triangles: RENAG; Circles - RGP; Hexagons: Spanish networks (Topo-Iberia, RGAN, CATNET, EPSH). Symbols are color-coded according to time series length.
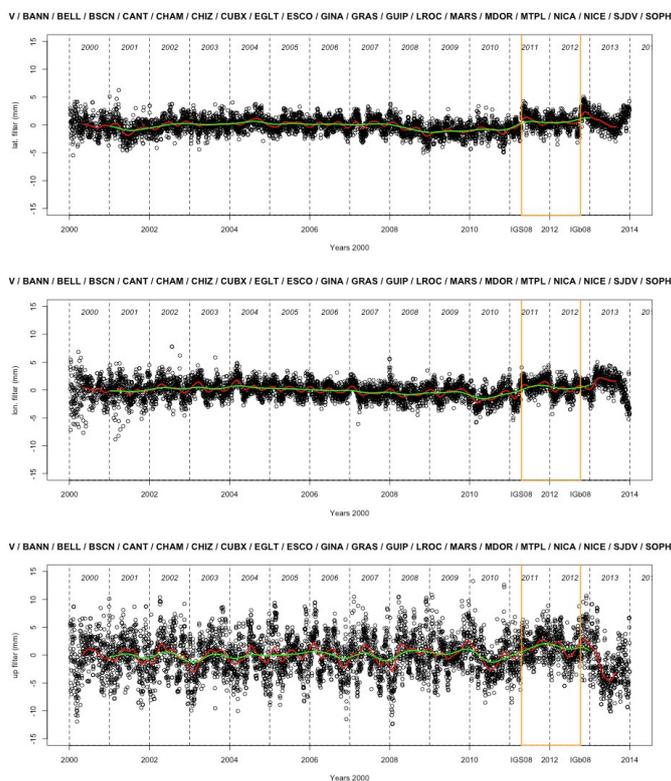
Figure 2: Common-mode stacked filter. Black circles show daily positions. Red and green curves show 1 month and 1 year time-average. Yellow vertical lines show the IGS05 – IGS08 and the IGS08 – IGb08 transitions.
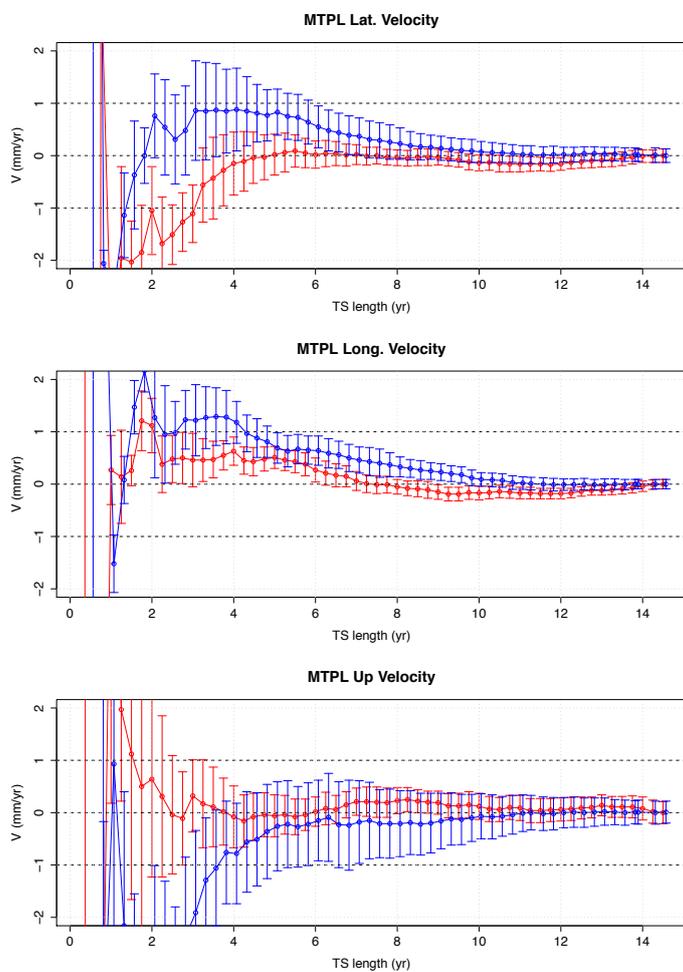
Figure 3: Velocity convergence for the station MTPL for the forward (red) and backward (blue) analyses.
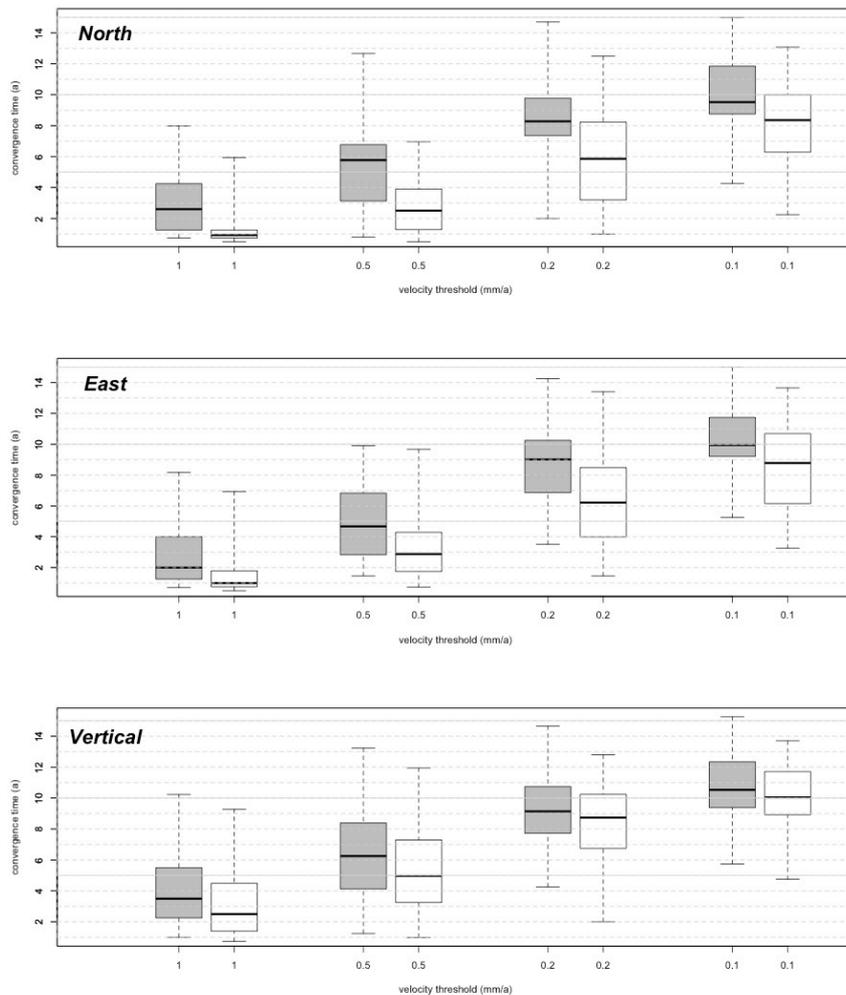
Figure 4: Whisker plots of convergence time for four velocity thresholds (1.0, 0.5, 0.2, and 0.1 mm/yr). Thick bars, boxes, and dashed bars represent the median, quartile (25% and 75%) and extreme values of the distributions for the 44 stations with at least 10 years of data. Grey and white whisker plots correspond to unfiltered (raw) and filtered (with common-mode correction) data.
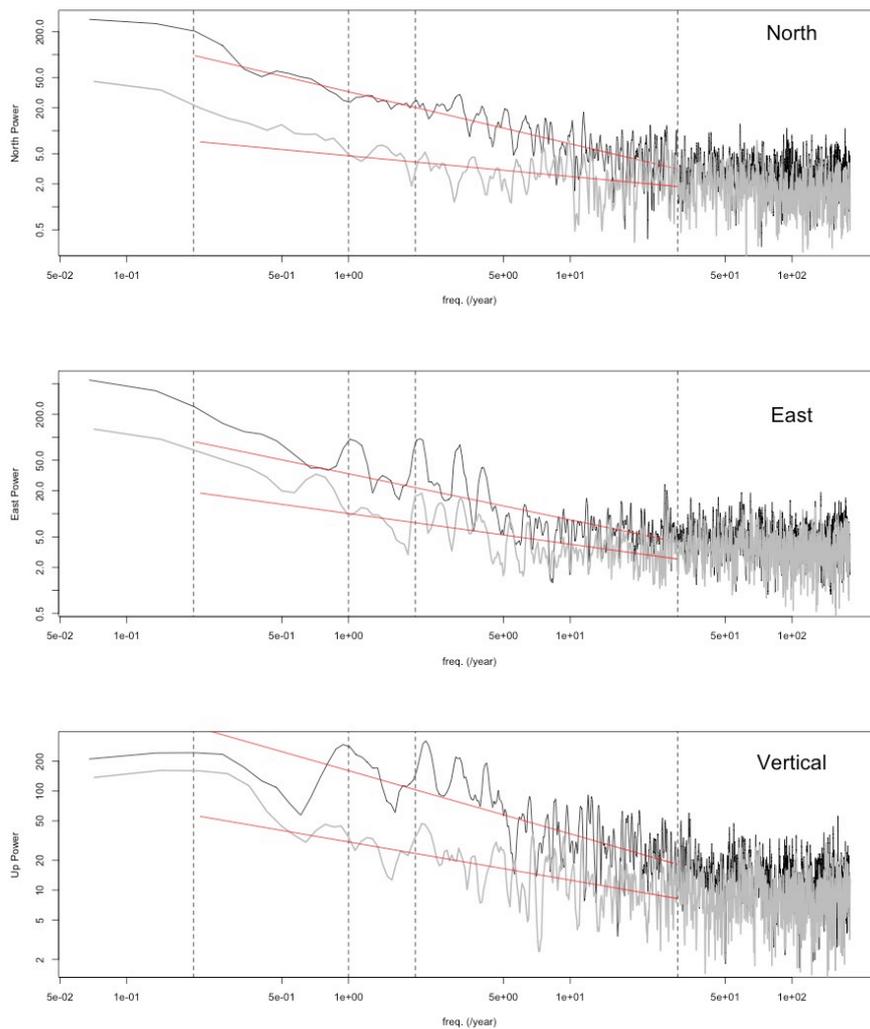
Figure 5: Noise spectra for site MTPL. Spectra derived form the unfiltered time series are in black, those for the filtered time-series are in grey. The red lines represent the best spectral models used for the uncertainty analyses.
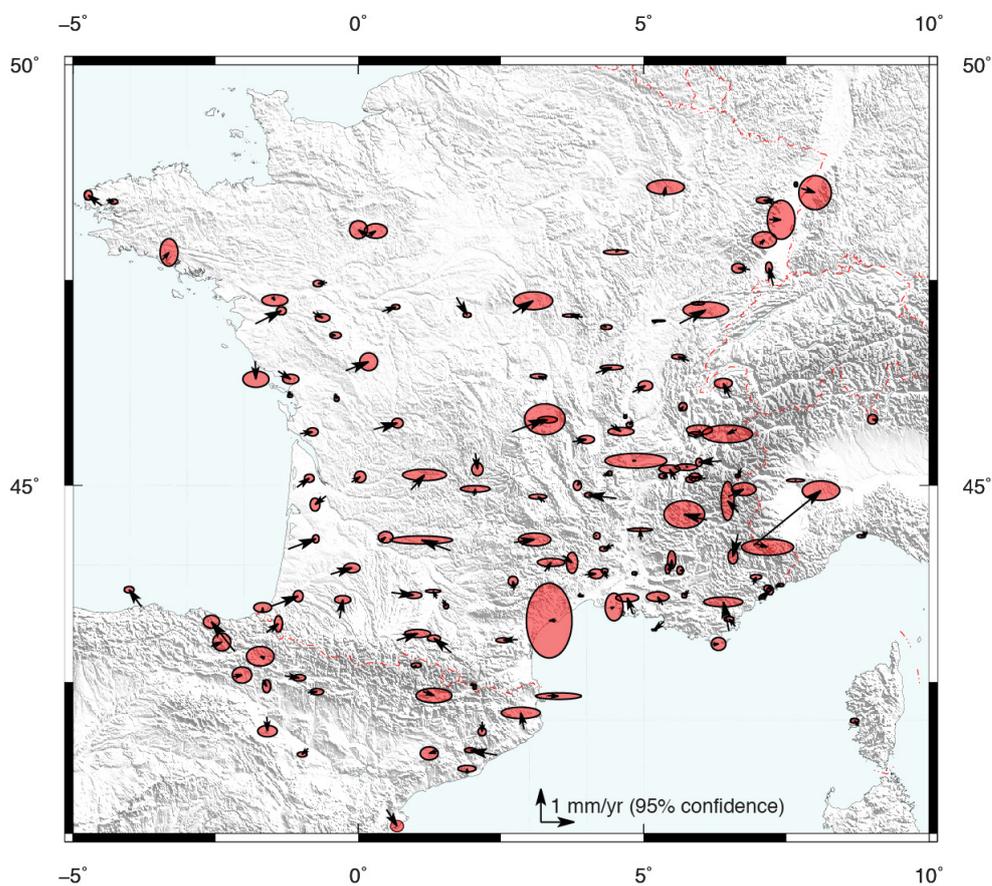
Figure 6: Horizontal velocities for stations with time series longer than 5 years in a regional (Western Europe) reference frame.
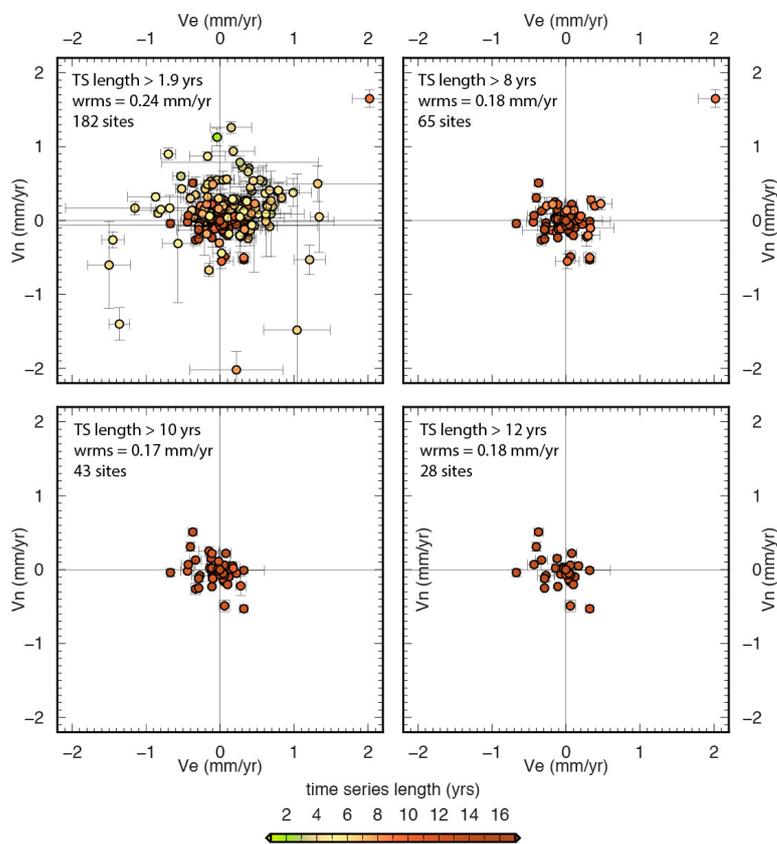
Figure 7: East versus North components of the residuals relative to a regional reference, color-coded based on the time series lengths.
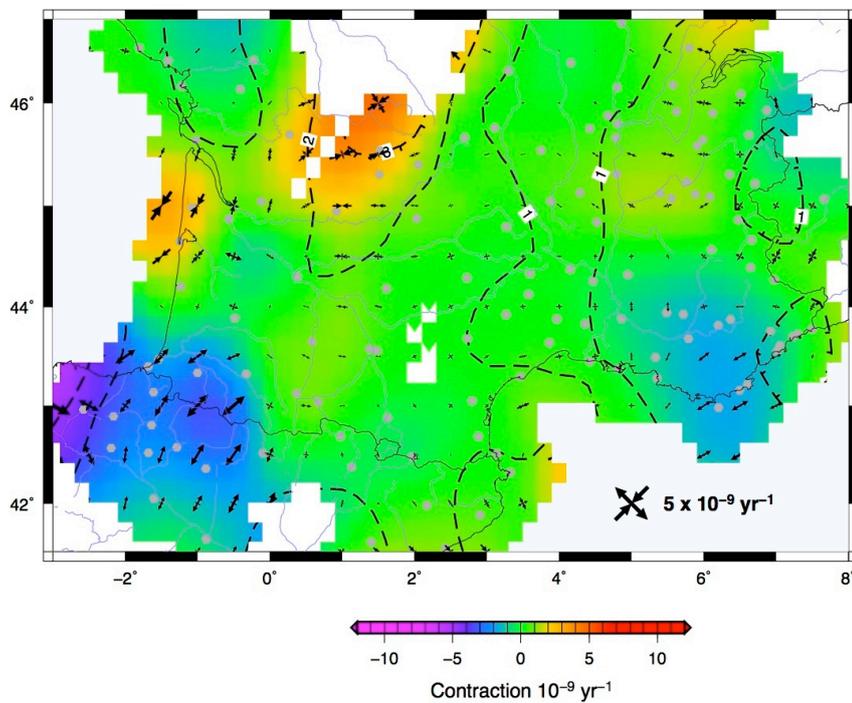
Figure 8: Smoothed horizontal strain rate field for the Western Alps and Pyrenees region. Dashed lines are strain rate standard error.
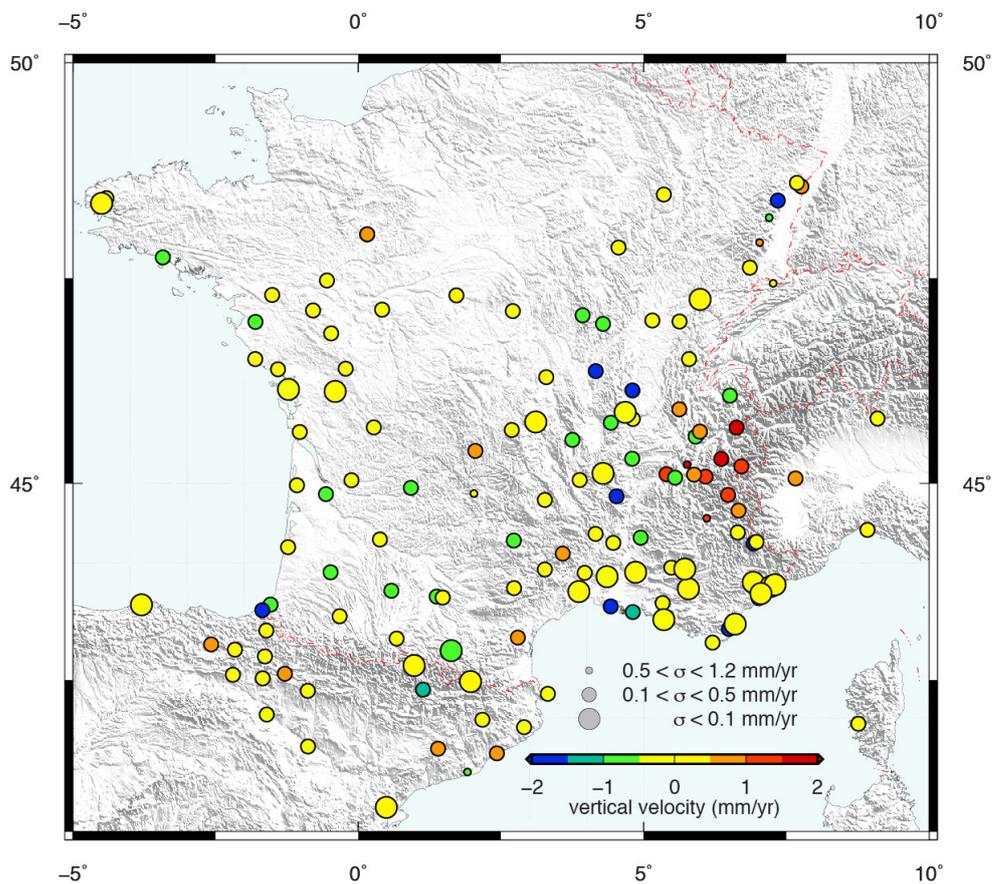
Figure 9: Vertical velocities for stations with time series longer than 5 years in the IGS08 reference frame (see table 3 for the site list).
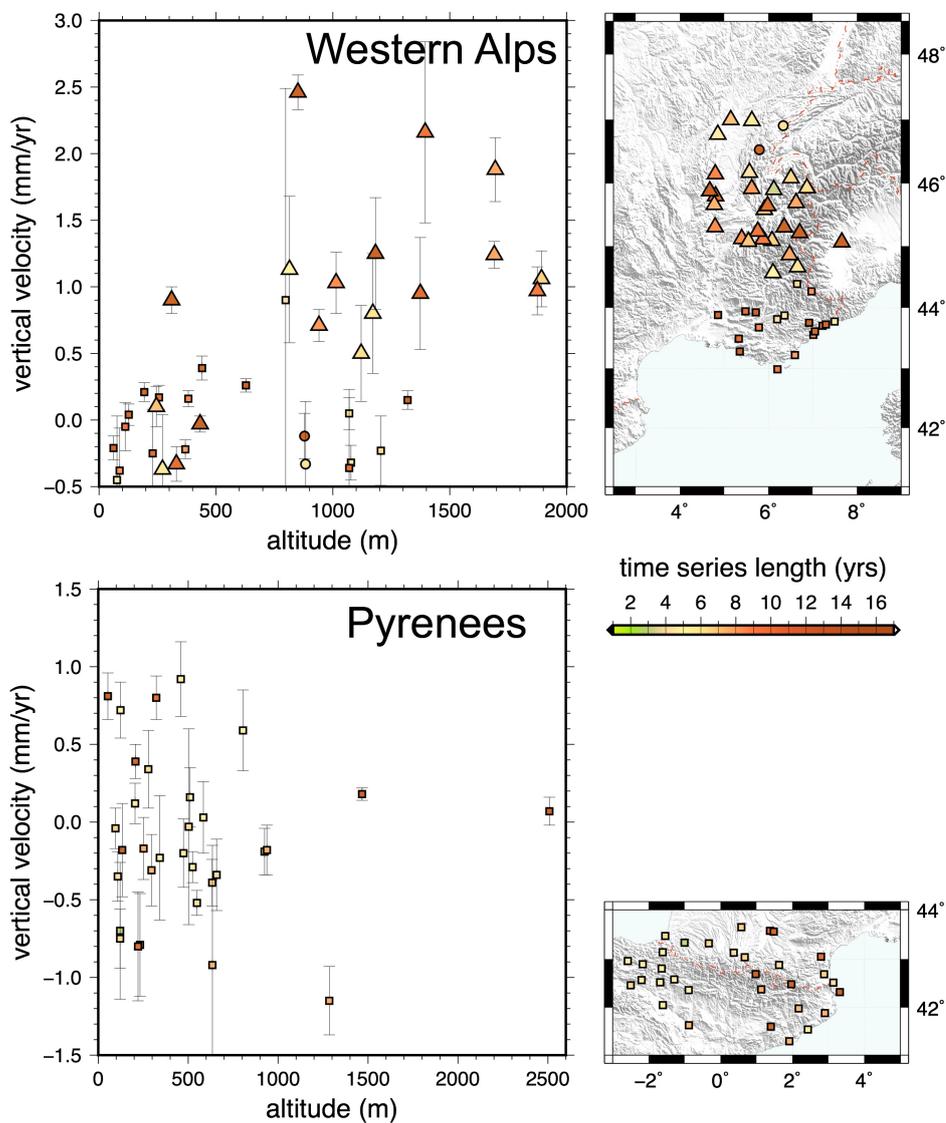
Figure 10: Vertical velocities, color-coded based on the time series length, versus site elevations for stations located in the Western Alps and the Pyrenees.

Table 1: Average offsets associated with the IGS reference frame transitions

	Raw data	Filtered data	Raw data	Filtered data
	IGS05 – IGS08	IGS05 – IGS08	IGS08 – Igb08	IGS08 – Igb08
North average (mm)	2.4	0.4	1.9	0.9
North standard deviation (mm)	0.9	0.8	0.9	0.8
East average (mm)	2.0	0.3	1.5	0.6
East standard deviation (mm)	1.0	1.1	1.1	1.1
Up average (mm)	3.0	-0.1	-3.1	-0.9
Up standard deviation (mm)	2.3	2.2	2.5	1.1

Table 2: Residuals between our velocity solution and the ITRF2008 velocities (Altamimi et al., 2011).

Site	East component (mm/yr)	North component (mm/yr)	Vertical component (mm/yr)
AJAC	0.07	0.12	-0.03
BRST	0.21	-0.18	-0.02
CHIZ	-0.01	0.37	0.47
GRAS	0.02	-0.14	0.25
LROC	-0.09	0.08	-0.28
MARS	0.06	0.04	0.66
SJDV	-0.10	0.08	0.24
TLSE	0.08	0.17	0.05
mean (mm/yr)	0.07	0.03	0.17
standard deviation (mm/yr)	0.17	0.10	0.30

Table 3: Site locations and velocities in a regional (Western Europe) reference frame as determined in this study by minimizing the velocities of the 61 sites indicated by an asterisk. East, north and vertical GPS velocity components (V_E, V_N, V_{Up}) and 1σ uncertainties (σ_E, σ_N, σ_{Up}) are given in mm/yr. "Dur." correspond to the length of the time series.

Site name	Lon. (˚E)	Lat. (˚N)	Alt. (m)	V_E (mm/yr)	V_N (mm/yr)	V_{Up} (mm/yr)	σ_E (mm/yr)	σ_N (mm/yr)	σ_{Up} (mm/yr)	Dur. (yr)
AGDE*	3.4664	43.2964	65.8	-0.21	-0.01	-0.50	0.28	0.46	0.18	6.29

AICI	-1.0014	43.3356	121.4	0.69	0.09	-0.70	0.45	0.58	0.44	2.86
AIGL*	3.5813	44.1214	1618.8	0.28	-0.22	0.98	0.07	0.13	0.25	11.31
AJAC*	8.7626	41.9275	98.8	-0.12	0.15	0.29	0.05	0.03	0.12	13.94
ALPE	6.0835	45.0866	1892.3	-0.32	0.04	1.06	0.07	0.05	0.21	6.81
ALSA	-2.1640	42.8920	584.2	-0.70	0.90	0.03	0.10	0.08	0.23	5.35
ALUY	3.6268	47.0419	324.1	-0.04	1.13	-0.27	0.07	0.12	0.47	1.94
AMB2	3.7501	45.5406	617.6	0.42	0.07	-0.77	0.10	0.05	0.25	6.16
ANCY	6.1233	45.9007	528.8	0.39	0.71	-1.00	0.23	0.08	0.19	3.16
ANGE*	-0.5479	47.4719	106.1	-0.27	-0.03	-0.06	0.06	0.04	0.37	9.90
ANGL*	-1.4061	46.4056	56.7	0.38	-0.24	0.00	0.10	0.06	0.15	6.78
ASIN	-0.0990	42.5170	1694.9	0.17	0.29	1.81	0.11	0.06	0.58	4.99
ATST	9.3360	42.1683	740.4	-0.53	0.60	-1.81	0.11	0.05	0.33	3.18
AUBU	7.1967	48.2169	1151.9	0.36	-0.01	-0.71	0.17	0.24	0.79	5.49
AUCH	0.5806	43.6495	232.0	0.67	-0.08	-0.79	0.10	0.04	0.33	6.78
AUTN*	4.2890	46.9538	353.6	0.10	-0.04	-0.89	0.07	0.03	0.24	8.71
AVEL	0.7510	41.8820	682.7	0.22	-2.02	3.11	0.63	0.25	0.62	7.89
AXPV*	5.3332	43.4912	229.4	-0.15	0.25	-0.25	0.14	0.06	0.33	11.27
BACT	6.6496	44.3877	1205.1	-0.15	-0.67	-0.23	0.06	0.09	0.26	6.39
BANN	4.1563	44.3692	357.6	0.04	0.00	0.40	0.04	0.04	0.45	10.49
BARY	0.6719	43.0357	633.5	0.63	0.21	-0.39	0.16	0.05	0.15	6.77
BAUB	3.9670	43.8769	210.9	0.34	0.03	0.43	0.09	0.06	0.38	5.43
BEA2	3.1367	42.5153	108.2	1.34	0.05	-0.35	0.12	0.48	0.16	4.14
BELL*	1.4000	41.6000	53.4	-0.27	-0.08	0.81	0.11	0.08	0.15	13.98
BIAZ	-1.5369	43.4720	121.4	0.83	0.31	-0.75	0.06	0.07	0.19	6.35
BLFT	6.8585	47.6259	416.5	-0.35	0.04	0.16	0.08	0.06	0.45	6.63
BLGN	5.5741	46.1718	544.7	-0.04	0.55	-3.40	0.18	0.04	0.43	4.26
BLIX	6.3667	43.8735	1077.2	0.22	0.29	-0.32	0.06	0.07	0.13	4.68
BRDO	9.4749	42.7746	69.5	-0.12	0.49	-1.89	0.04	0.13	0.77	3.14
BRES*	-0.4735	46.8397	245.2	0.13	0.00	-0.07	0.07	0.04	0.18	10.24
BRST	-4.4966	48.3805	65.8	-0.40	0.31	0.11	0.05	0.06	0.06	13.98
BSCN*	5.9894	47.2469	359.5	-0.07	-0.06	0.39	0.08	0.02	0.07	12.21
BUAN	5.3536	48.4862	416.3	0.05	0.28	0.47	0.23	0.09	0.29	6.13
CACI*	3.9328	47.0569	610.2	-0.36	0.05	-0.63	0.10	0.02	0.35	7.06
CAMP	8.7908	41.9182	60.8	0.38	0.66	-0.84	0.13	0.08	0.52	3.63
CANT	-3.8000	43.4700	99.0	-0.37	0.51	0.13	0.06	0.04	0.07	13.00
CARQ*	-1.5091	47.2990	88.1	0.08	-0.10	0.07	0.16	0.07	0.24	6.52
CASS	2.9040	41.8830	251.8	-0.10	0.49	-0.17	0.24	0.07	0.20	7.74
CAUS	1.6150	44.1816	227.0	-0.87	0.32	-2.62	0.38	0.05	1.20	5.00
CBRY	5.9092	45.5813	324.7	0.00	0.13	-0.54	0.09	0.03	0.18	7.16
CHAL	4.8587	46.7673	234.1	0.62	0.03	-2.24	0.25	0.12	0.61	4.71
CHAM*	5.8811	45.1107	1874.6	-0.10	-0.09	0.97	0.06	0.04	0.18	10.03
CHAS*	4.5594	47.8627	299.4	-0.08	-0.08	0.06	0.15	0.03	0.21	7.52

CHIZ*	-0.4077	46.1335	113.2	0.05	-0.16	0.18	0.03	0.03	0.03	13.19
CHMX	6.8730	45.9262	1120.8	-1.50	-0.60	0.50	0.29	0.59	0.36	6.33
CHRN*	4.8617	43.8814	126.8	-0.04	0.03	0.04	0.03	0.02	0.08	13.17
CHTL	6.3586	45.3041	850.3	-0.67	-0.04	2.46	0.04	0.05	0.13	13.98
CLAP	6.9271	44.2484	1370.0	2.02	1.65	-1.67	0.23	0.12	0.41	8.91
CLFD	3.1111	45.7610	473.6	0.35	0.13	0.18	0.12	0.04	0.08	7.15
CNNS	7.0157	43.5546	88.0	0.34	0.28	-0.38	0.04	0.05	0.32	8.59
COMO*	9.0956	45.8022	292.3	-0.15	0.04	-0.21	0.06	0.06	0.12	9.78
COUT	-0.1176	45.0410	81.8	0.26	0.16	-0.34	0.07	0.07	0.23	6.28
CRAL	0.3672	43.1284	658.4	0.30	0.73	-0.34	0.12	0.07	0.23	3.89
CREU	3.3200	42.3200	133.4	0.32	-0.01	-0.18	0.28	0.04	0.30	13.98
CUBX	-0.5664	44.8689	59.0	-0.33	-0.26	-0.91	0.06	0.08	0.19	11.24
DIJO	5.0651	47.3106	328.7	0.51	0.09	-0.34	0.13	0.10	0.31	4.71
DOJX	5.1605	48.3629	287.9	-0.57	-0.31	-0.41	0.21	0.80	0.36	5.43
EBRE	0.4920	40.8210	107.8	0.32	-0.50	0.06	0.08	0.07	0.08	8.72
EGLT	2.0520	45.4034	667.0	0.06	-0.49	0.69	0.07	0.08	0.20	12.21
EOST	7.7625	48.5798	213.4	0.41	-0.13	0.72	0.20	0.21	0.40	6.62
EPSH	-0.4480	42.1190	522.8	-1.36	-1.40	4.42	0.14	0.22	1.44	4.56
ERCK	7.3642	48.8730	296.2	-0.14	0.11	0.15	0.07	0.06	0.44	4.66
ESAB*	4.7979	45.3071	207.7	0.11	0.00	-0.78	0.38	0.09	0.31	8.87
ESCO*	0.9800	42.6900	2508.4	0.06	0.06	0.07	0.06	0.03	0.09	13.98
EZEV	7.4973	43.7744	76.7	-0.15	0.46	-0.45	0.10	0.09	0.48	4.84
FCLZ*	5.9857	45.6432	1374.2	-0.02	0.11	0.95	0.16	0.06	0.42	12.00
FERR	-1.2488	44.6460	106.2	0.62	-0.01	-3.85	0.92	0.48	1.50	6.72
FJCP	2.7949	43.0482	322.7	-0.44	-0.02	0.80	0.09	0.03	0.14	11.19
FLRC	3.5945	44.3253	607.9	-1.45	-0.26	-0.32	0.15	0.11	0.19	4.86
FRTT	5.5663	47.6803	373.5	-0.10	-0.06	-1.06	5.56	0.30	2.04	5.43
FUEN	-0.8850	42.3600	924.8	0.28	0.03	-0.19	0.08	0.04	0.15	5.15
GARR	1.9140	41.2930	634.5	-0.02	0.16	-0.92	0.11	0.04	0.77	7.72
GDIJ	5.0447	47.3327	315.2	0.58	0.53	-0.24	0.32	0.21	0.28	3.19
GENO*	8.9211	44.4194	152.7	-0.19	-0.13	0.06	0.05	0.02	0.17	8.43
GINA	5.7870	43.6757	382.0	-0.13	-0.15	0.16	0.03	0.03	0.06	9.02
GLRA	4.5241	44.8393	813.9	-0.84	0.10	-1.62	0.05	0.03	0.27	5.86
GRAS*	6.9206	43.7547	1319.3	0.08	0.22	0.15	0.07	0.03	0.07	13.98
GRJF	1.5139	45.3029	458.6	0.43	0.40	0.18	0.14	0.08	0.72	3.27
GRON	2.7082	47.1067	222.8	0.61	0.37	-0.48	0.24	0.11	0.25	5.53
GUIL	6.6619	44.6622	1171.2	-0.33	0.35	0.80	0.08	0.24	0.45	6.13
GUIP*	-4.4118	48.4446	154.7	0.22	-0.05	-0.45	0.05	0.03	0.14	11.20
ILBO*	0.4179	47.1246	90.5	0.41	0.14	-0.35	0.05	0.03	0.40	6.63
JOUX*	5.7958	46.5287	878.9	-0.33	0.13	-0.12	0.08	0.03	0.17	13.70
LACA	2.7276	43.6810	1326.3	-0.03	0.27	0.06	0.06	0.06	0.16	7.48
LBUG	0.9211	44.9454	266.5	0.41	0.45	-0.78	0.27	0.07	0.33	6.35

LCAU*	-1.0755	44.9782	73.7	0.37	0.27	-0.50	0.06	0.05	0.14	7.52
LEBE*	5.6246	45.9161	940.5	0.11	0.14	0.71	0.05	0.05	0.12	8.45
LFAZ*	5.3990	45.1166	1014.0	-0.11	0.00	1.03	0.05	0.03	0.23	8.78
LGAR*	0.3789	44.2974	136.1	0.17	0.13	-0.34	0.09	0.07	0.17	6.30
LLIV*	1.9700	42.4800	1466.8	0.12	-0.10	0.18	0.02	0.03	0.04	13.98
LNDA	-2.5780	42.9600	804.4	0.32	0.13	0.59	0.11	0.11	0.26	5.10
LOSA	-2.1950	42.5680	510.3	0.27	0.05	0.16	0.12	0.10	0.19	5.36
LROC*	-1.2193	46.1589	57.9	0.04	-0.13	-0.02	0.03	0.02	0.04	12.07
LUCE	7.2682	47.4384	741.6	-0.13	0.53	-0.19	0.04	0.07	0.51	6.16
LUCI	9.5309	42.3863	63.7	0.54	0.55	-0.26	0.15	0.13	0.13	3.63
LUMI	8.8274	42.6029	57.0	0.18	0.94	-0.76	0.29	0.07	0.33	3.63
LURI	9.4759	42.8884	54.2	0.15	1.26	-0.71	0.28	0.08	0.58	3.54
MACH	-1.8029	46.9782	64.6	0.78	0.39	-0.51	0.06	0.05	0.11	6.16
MAKS	7.0315	47.9230	1237.2	0.14	0.14	0.50	0.15	0.10	0.78	6.64
MAN2	0.1553	48.0186	168.0	0.26	0.16	-0.34	0.14	0.09	0.13	5.80
MANS*	0.1553	48.0186	168.0	-0.26	0.20	0.62	0.11	0.11	0.45	8.13
MARG	6.5107	46.0844	524.2	-0.20	0.43	-0.63	0.11	0.06	0.28	6.63
MARS	5.3538	43.2788	61.8	-0.29	-0.25	-0.21	0.03	0.01	0.09	13.98
MATA	2.4290	41.5400	123.6	-0.80	0.15	0.72	0.07	0.03	0.18	5.14
MDOR*	4.8090	45.7990	330.6	-0.10	-0.12	-0.33	0.04	0.03	0.13	11.21
MICH*	5.7174	43.9242	628.2	-0.14	0.02	0.26	0.04	0.05	0.05	13.98
MIMZ	-1.2283	44.2006	71.7	0.83	0.31	0.07	0.04	0.05	0.11	6.63
MNBL	6.8061	47.4958	413.1	-0.29	-0.08	-0.43	0.27	0.09	0.39	4.71
MODA*	6.7101	45.2138	1182.3	-0.11	-0.23	1.25	0.03	0.02	0.42	13.98
MOGN	4.8029	46.1483	233.0	0.39	0.20	-1.74	0.09	0.06	0.15	9.19
MONB	4.3381	47.6190	303.9	0.46	-0.07	-0.42	0.86	0.63	0.87	4.10
MORN	0.2725	45.6939	231.1	0.71	0.19	-0.26	0.07	0.06	0.14	5.89
MSGT	1.6294	42.8796	548.6	-0.52	0.43	-0.52	0.08	0.04	0.08	6.10
MSMM	6.1998	43.8107	797.8	0.45	0.54	0.90	0.17	0.04	1.59	4.10
MSRT	1.5214	45.5414	566.2	-0.40	0.30	-0.49	0.13	0.07	0.69	3.86
MTDM	-0.4849	43.8827	133.9	0.64	0.19	-0.94	0.10	0.06	0.24	6.32
MTPL*	3.8648	43.6374	120.3	0.06	-0.07	0.02	0.03	0.01	0.04	13.89
NICA*	7.2273	43.7033	256.5	-0.09	0.00	0.17	0.05	0.04	0.09	11.04
NICE*	7.3003	43.7255	440.6	0.17	0.05	0.39	0.04	0.02	0.09	13.04
NIME*	4.3569	43.8286	106.1	-0.07	0.23	-0.40	0.04	0.03	0.03	7.79
ORON	-1.6090	43.1390	204.9	0.36	0.26	0.12	0.05	0.10	0.13	5.36
PALI	4.8105	43.3760	60.5	-0.17	0.49	-1.19	0.14	0.05	0.20	6.06
PAMP	-1.6360	42.8060	524.5	-0.14	0.06	-0.29	0.17	0.12	0.10	5.36
PERP	2.8820	42.6891	95.9	1.32	0.50	-0.04	1.30	0.24	0.13	6.78
PIAA	8.6293	42.2350	543.3	0.27	0.79	-2.40	1.06	0.08	1.24	3.18
PIAN	9.0561	41.4947	153.1	1.21	-0.53	-0.46	0.21	0.20	0.52	3.63
PIMI	0.1426	42.9364	2923.4	1.78	-5.46	2.29	1.35	11.05	2.11	3.22

PLOE	-3.4273	47.7461	74.0	0.19	0.21	-0.74	0.11	0.17	0.19	7.04
POBU	4.1603	46.3828	420.8	0.48	0.17	-1.92	0.14	0.03	0.39	5.97
PQRL*	6.2061	42.9833	112.3	0.18	0.02	-0.05	0.09	0.08	0.18	10.29
PRNY	6.3383	46.9049	883.6	-1.15	0.17	-0.33	0.94	0.09	0.47	6.16
PUYA	6.4789	44.8577	1690.3	0.47	0.23	1.24	0.15	0.08	0.10	8.08
PUYV*	3.8789	45.0436	710.3	-0.07	-0.11	-0.13	0.05	0.06	0.12	9.30
RABU*	6.9771	44.2678	2551.9	0.33	-0.10	0.30	0.32	0.10	0.25	8.66
RAYL	6.4939	43.1605	336.3	-0.17	0.87	-2.07	0.24	0.06	0.32	5.21
RIOJ	-2.5000	42.4600	503.1	1.04	-1.48	-0.03	0.45	2.11	0.63	6.47
ROSD*	6.6282	45.6915	1694.5	-0.28	-0.13	1.88	0.31	0.11	0.24	8.04
ROTG	-3.9657	48.7184	56.1	-0.38	0.14	-0.51	0.78	0.12	0.44	4.35
ROYA*	-1.0244	45.6386	69.0	0.38	0.06	0.04	0.07	0.05	0.15	6.78
RST2	5.4837	43.9410	1069.8	0.01	0.30	0.05	0.05	0.11	0.12	6.06
RSTL*	5.4837	43.9410	1069.9	-0.11	0.02	-0.36	0.03	0.06	0.59	11.43
SABL	-1.8058	46.5300	56.7	0.02	-0.55	0.40	0.16	0.10	0.15	9.91
SANG	-1.2870	42.5800	459.2	0.43	-0.06	0.92	0.08	0.04	0.24	5.36
SARI	9.4025	41.8583	57.2	0.04	0.55	-0.98	0.15	0.12	0.15	3.63
SAUV*	4.4675	44.2554	406.4	-0.29	-0.12	-0.17	0.05	0.03	0.14	13.99
SBAR	2.1740	41.9800	937.9	-0.01	-0.30	-0.18	0.05	0.05	0.16	7.72
SCDA*	3.2675	44.7945	1115.3	-0.21	0.16	-0.50	0.11	0.03	0.22	6.61
SCLP	4.4264	45.7503	703.7	0.30	-0.20	-0.63	0.16	0.05	0.18	8.44
SCOA	-1.6800	43.4000	59.5	0.01	0.14	-2.77	0.11	0.06	0.19	8.02
SEUR*	5.1515	46.9943	245.1	0.19	0.05	0.10	0.08	0.01	0.15	7.28
SJDV*	4.6766	45.8790	432.4	0.00	-0.07	-0.03	0.02	0.02	0.06	13.98
SJPL	2.6896	45.6632	1029.1	0.99	0.38	-0.05	0.25	0.19	0.36	5.21
SLVT	3.2683	43.9198	811.8	0.19	0.27	0.25	0.17	0.05	0.16	6.29
SMLE	-0.2219	46.4112	170.5	0.69	0.27	-0.13	0.11	0.11	0.10	6.63
SMTG	-2.0275	48.6411	57.7	0.67	0.41	-0.40	0.35	0.15	1.13	3.87
SOPH*	7.0544	43.6114	193.3	0.04	-0.05	0.21	0.04	0.02	0.07	12.96
SORI	1.1330	42.3750	1284.5	0.33	-0.12	-1.15	0.22	0.09	0.22	7.89
SOUS	2.0271	44.8746	597.7	0.04	0.20	0.11	0.18	0.04	0.56	6.63
STEY*	5.7618	45.2352	1394.9	-0.03	-0.02	2.16	0.14	0.04	0.68	10.46
STJ9*	7.6838	48.6217	237.2	-0.03	0.01	0.23	0.02	0.03	0.14	13.98
STMR	4.4216	43.4491	56.2	0.10	0.04	-2.23	0.11	0.17	0.29	5.72
STPS*	3.2940	46.3084	299.7	-0.24	0.09	0.07	0.10	0.03	0.21	7.28
STV2	6.1062	44.5669	814.7	-0.68	0.17	1.13	0.25	0.17	0.55	5.04
TAFA	-1.6770	42.5210	473.9	0.12	-0.18	-0.20	0.05	0.08	0.22	5.36
TENC*	4.2875	45.1246	936.5	0.20	0.06	0.05	0.03	0.03	0.09	9.53
TLMF*	1.3751	43.5746	221.1	-0.11	0.22	-0.80	0.09	0.02	0.35	11.53
TLSE*	1.4800	43.5600	207.2	0.10	-0.20	0.39	0.03	0.03	0.11	12.98
TORI*	7.6613	45.0634	310.4	0.00	0.00	0.90	0.11	0.02	0.10	13.98
TOUL	1.4810	43.5610	207.1	-5.75	4.64	-0.41	1.95	1.76	1.15	0.99

TREM*	-0.7940	47.1159	166.5	0.29	-0.17	0.05	0.09	0.05	0.15	6.39
TRMO	2.7248	44.2854	810.9	0.62	0.09	-0.91	0.20	0.08	0.30	5.42
TROP*	6.6010	43.2195	369.3	-0.18	0.22	-0.22	0.06	0.03	0.07	8.31
TUDE	-1.6030	42.0490	342.0	0.02	-0.44	-0.23	0.12	0.07	0.40	5.36
UNME	-0.3257	43.3216	278.7	0.09	0.56	0.34	0.10	0.05	0.25	6.54
VAUD	5.6269	46.9812	271.5	0.79	0.41	-0.37	0.28	0.10	0.41	5.86
VFCH	1.7197	47.2942	153.3	0.32	-0.53	0.39	0.05	0.03	0.11	12.31
VILR	5.5518	45.0725	1076.7	-0.17	0.32	-0.82	0.13	0.05	0.13	7.06
VISN	4.9492	44.3199	245.8	-0.02	0.30	-0.51	0.15	0.02	0.20	6.39
VOUR*	4.7807	45.6616	324.9	0.42	0.10	-2.77	0.54	0.32	0.90	7.66
VSOL	6.0666	47.6894	321.9	0.27	-0.20	-0.82	0.12	0.23	0.25	4.71
WLBH	7.3513	48.4152	819.0	-0.43	0.07	-2.61	0.09	0.04	0.36	13.18
ZARA*	-0.8800	41.6300	296.1	-0.18	-0.18	-0.31	0.06	0.03	0.23	7.58